Stability and nucleation of dipole strings in uniaxial chiral magnets

Vladyslav M. Kuchkin,[1,*] Nikolai S. Kiselev,[2] Andreas Haller,[1] Štefan Liščák,[1] Andreas Michels,[1] and Thomas L. Schmidt[1]

[1]*Department of Physics and Materials Science, University of Luxembourg, L-1511 Luxembourg, Luxembourg*

[2]*Peter Grünberg Institute, Forschungszentrum Jülich and JARA, 52425 Jülich, Germany*

(Received 30 January 2025; revised 1 April 2025; accepted 24 April 2025; published 6 May 2025)

We report on the stability of the magnetic dipole string (DS), a three-dimensional magnetic texture formed by two coupled Bloch points with opposite topological charges, separated by an equilibrium distance. Previous studies demonstrated the stability of such configurations through geometric confinement or coupling with local perturbations in the magnetization field, such as skyrmion strings or dislocations in helical modulations. Here, we show that, in uniaxial chiral magnets, an isolated DS remains stable in an unperturbed vacuum, thus representing a true three-dimensional soliton. The phase diagram illustrates the stability of the DS embedded in the conical or helical phases across a broad range of material parameters and external magnetic fields. Using the geodesic nudged elastic band method applied to a regularized micromagnetic model, we demonstrate that isolated DSs are protected from collapse by an energy barrier. Stochastic spin-lattice simulations demonstrate that DSs can spontaneously nucleate during in-field annealing. This work aims to stimulate the experimental observation of DSs and further exploration of uniaxial chiral magnets.

DOI: 10.1103/PhysRevB.111.174410

I. INTRODUCTION

Magnetic skyrmions [1] are two-dimensional (2D) topological solitons that can be stabilized in various magnetic systems [2–4]. Their unique particlelike properties have garnered significant interest for potential applications (see, e.g., Refs. [5–7] and references therein).

In bulk three-dimensional (3D) samples, magnetic skyrmions can form intricate filamentary textures of nontrivial topology. For example, 3D skyrmion strings can braid [8], hybridize [9], cluster into bundles [10], or even host hopfion rings [11]. Typically, these strings penetrate the entire thickness of a sample. However, there are exceptions, such as configurations in which a skyrmion string emerges from the surface and terminates within the sample volume by a singularity, a so-called Bloch point (BP) [12,13]. These statically stable configurations are referred to as chiral bobbers [14–16].

The magnetic textures studied in this work can be viewed as fragments of skyrmion strings that begin and terminate within the crystal volume, encompassing two BPs, as illustrated in Fig. 1(a). In the literature, these configurations are referred to as magnetic dipole strings (DSs) [17], torons [18], cocoons [19], globules [20], or monopole-antimonopole pairs [21,22].

Previous studies have shown that the stabilization of DSs can be achieved through geometric confinement [23], artificial surface anisotropy [24,25], or coupling to auxiliary textures, such as skyrmion strings, conical edge dislocations [17], or conical screw dislocations [26]. However, DS configurations stabilized by these methods are constrained by their environments and do not represent true 3D magnetic solitons capable of free motion in all spatial directions. In this work, we introduce a class of magnetic crystals where DSs emerge as freely mobile, true 3D solitons stabilized purely by local interactions. We show that such DSs can be easily nucleated, detected, and moved efficiently by external stimuli.

The paper is organized as follows. In Sec. II we introduce the micromagnetic Hamiltonian. Section III A features the results on the phase diagram of DSs; Sec. III B addresses the stability range of DSs; Sec. III C is concerned with the nucleation properties; Sec. III D discusses the results for the energy barriers obtained with the regularized geodesic nudged elastic band method (RGNEB); Sec. III E discusses possibility of nucleation of an isolated DS; and Sec. III F addresses the current-induced motion of DSs. Finally, Sec. IV summarizes the main findings of this study. The Supplemental Material [27] provides further details on the derivation of the cone-to-ferromagnetic transition, MUMAX3 scripts for the DS ansatz in cone and helix phases, details of the RGNEB method, and the velocity projection optimization algorithm.

II. MODEL

We consider a chiral ferromagnet with bulk-type Dzyaloshinskii-Moriya interaction [28,29] (DMI) and hard-axis (easy-plane) anisotropy:

$$\mathcal{E}(\mathbf{n}) = \int [\mathcal{A}(\partial_i \mathbf{n})^2 + \mathcal{D}\,\mathbf{n}\cdot\boldsymbol{\nabla}\times\mathbf{n} + U(\mathbf{n})]\mathrm{d}V, \qquad (1)$$

where $\mathcal{A}$ and $\mathcal{D}$ are the strengths of exchange and DMI, respectively; summation over subscript $i \in \{x, y, z\}$ is assumed. The potential term $U(\mathbf{n}) = -\frac{1}{2}M_\mathrm{s}\mathbf{B}_\mathrm{d}\cdot\mathbf{n} - M_\mathrm{s}B_\mathrm{ext}n_z + \mathcal{K}_\mathrm{u}n_x^2$

*Contact author: vladyslav.kuchkin@uni.lu

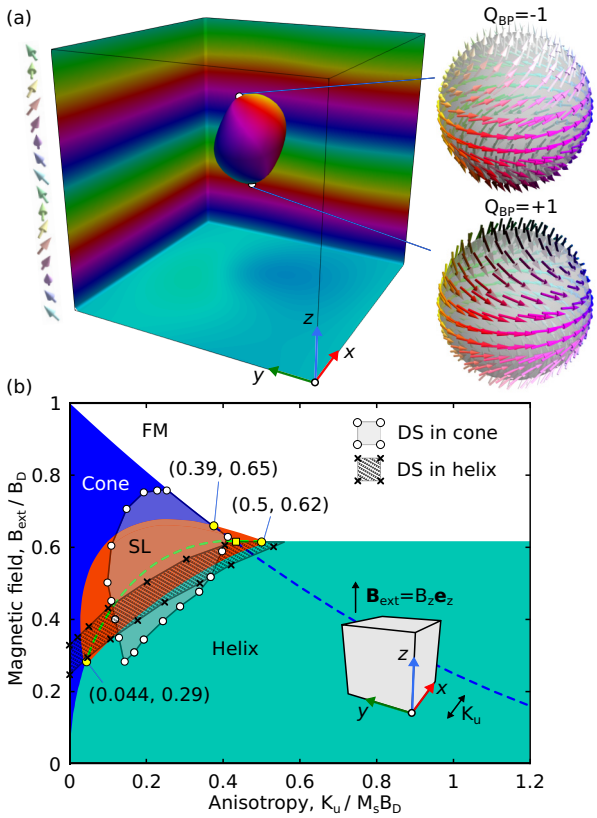

FIG. 1. (a) Stable DS solution in the cone phase obtained by direct energy minimization of Eq. (1) at $h = B_{\text{ext}}/B_{\text{D}} = 0.55$ and $u = \mathcal{K}_{\text{u}}/(M_{\text{s}}B_{\text{D}}) = 0.25$, visualized via the isosurface ($n_z = 0$). The inset highlights two Bloch points (BPs) with opposite topological charges [33]. The standard color code [34,35] is used throughout: white and black pixels indicate magnetic moments aligned parallel and antiparallel to the z axis, respectively, while red, green, and blue represent the azimuthal angle relative to the x axis. (b) State diagram for chiral magnets under an external field applied orthogonally to the hard axis of the magnetocrystalline anisotropy. The red region corresponds to the skyrmion lattice (SL), and the dashed green line marks the conditions where the metastable cone and helix phases have identical energies. The dashed blue line, instead, marks the critical field at which the cone saturates to a FM state. The two semitransparent regions indicate the stability domains of DSs within the cone and helix phases.

accounts for the demagnetizing field $\mathbf{B}_{\text{d}}$, the externally applied magnetic field $B_{\text{ext}} > 0$ along the z axis, and an easy-plane anisotropy $\mathcal{K}_{\text{u}} > 0$ with the hard axis along the x axis. A comprehensive analysis of the role of the anisotropy is very cumbersome and beyond the scope of the present paper. This aspect will be considered elsewhere.

For further convenience, we introduce the characteristic length scale $L_{\text{D}} = 4\pi\mathcal{A}/\mathcal{D}$ and the magnetic field $B_{\text{D}} = \mathcal{D}^2/(2\mathcal{A}M_{\text{s}})$ that correspond to the equilibrium period of the chiral modulations at $U(\mathbf{n}) = 0$ and to the saturation magnetic field at $\mathbf{B}_{\text{d}} = 0$ and $\mathcal{K}_{\text{u}} = 0$, respectively. Using these characteristic parameters, we can employ the dimensionless field $h = B_{\text{ext}}/B_{\text{D}}$ and anisotropy $u = \mathcal{K}_{\text{u}}/(M_{\text{s}}B_{\text{D}})$. In the following discussion, we ignore the presence of demagnetizing fields that usually introduce quantitative but not qualitative changes to most of the magnetic spin textures studied previously [8,14,30], especially for the bulk.

III. RESULTS

A. Phase diagram

Figure 1(b) presents the diagram of magnetic states for the model (1) in a scenario [31], where the external field is applied perpendicular to the hard axis (see bottom right inset). The ground state of the system is the spin spiral. It is common to distinguish spin spirals based on the orientation of their wave vector $\mathbf{q}$ relative to the applied magnetic field. In the case of $\mathbf{q} \parallel \mathbf{B}_{\text{ext}}$, the spin spiral is referred to as the cone, while for $\mathbf{q} \perp \mathbf{B}_{\text{ext}}$, it is typically referred to as the helix. The cone and helix can serve as a vacuum for ordinary and hybrid skyrmion strings [8,9], heliknotons [30,32], and 3D chiral droplets [9]. In Fig. 1(b), the regions of stable DSs submerged in the cone or helix phases are depicted by the gray semitransparent areas marked by circles (○) and crosses (×), respectively. Error bars for all points in the diagram do not exceed 10^{-3} for both h and u values, and are therefore smaller than the size of the symbols.

Let us briefly discuss the key aspects of the diagram shown in Fig. 1(b). In the isotropic case ($u = 0$), there are only two phases: the cone phase for $h < 1$ and the saturated or ferromagnetic (FM) state for $h > 1$. Similarly to the case of an easy-axis anisotropy [36], for hard-axis bulk chiral magnets, the phase diagram contains four phases [31]: cone, helix, skyrmion lattice (SL), and FM [Fig. 1(b)]. The equilibrium period of the cone phase in the case $u > 0$ depends on the magnetic field h and cannot be found analytically. On the other hand, by analyzing the Euler-Lagrange equations, one can derive the critical field h_1^{cr} at which the system saturates to the FM state:

$$h_1^{\text{cr}} = (1 - u/2)^2, \quad u \in [0, 2]. \tag{2}$$

For details, we refer the reader to the Supplemental Material I [27]. In the diagram Fig. 1(b), the function $h_1^{\text{cr}}(u)$ is marked by the dashed blue line.

The period of the helix is a function of h, but in our geometry, when $\mathbf{B}_{\text{ext}}$ is orthogonal to the hard anisotropy axis, it does not depend on u. Thus, the transition to the FM state can be found by analyzing a single 360°-domain wall state that corresponds to $h_2^{\text{cr}} = \pi^2/16$. Comparing the latter with (2), we find a critical anisotropy value of $u^{\text{cr}} = 1 - \pi/2$, corresponding to the triple point, cone-helix-FM (see square symbol in the diagram).

To investigate phase transitions between the cone, helix, and SL phases, we numerically minimized the Hamiltonian (1) using optimized parameters for each phase and compared their respective energies. These calculations were performed with the conjugate gradient method, enabling high-precision estimates of phase transitions and stability of the DS. Specifically, we identified three triple points corresponding to the cone-helix-SL, cone-FM-SL, and helix-FM-SL transitions, which in terms of (u, h) are located at $(0.044, 0.29)$, $(0.39, 0.65)$, and $(0.5, \pi^2/16)$, respectively.

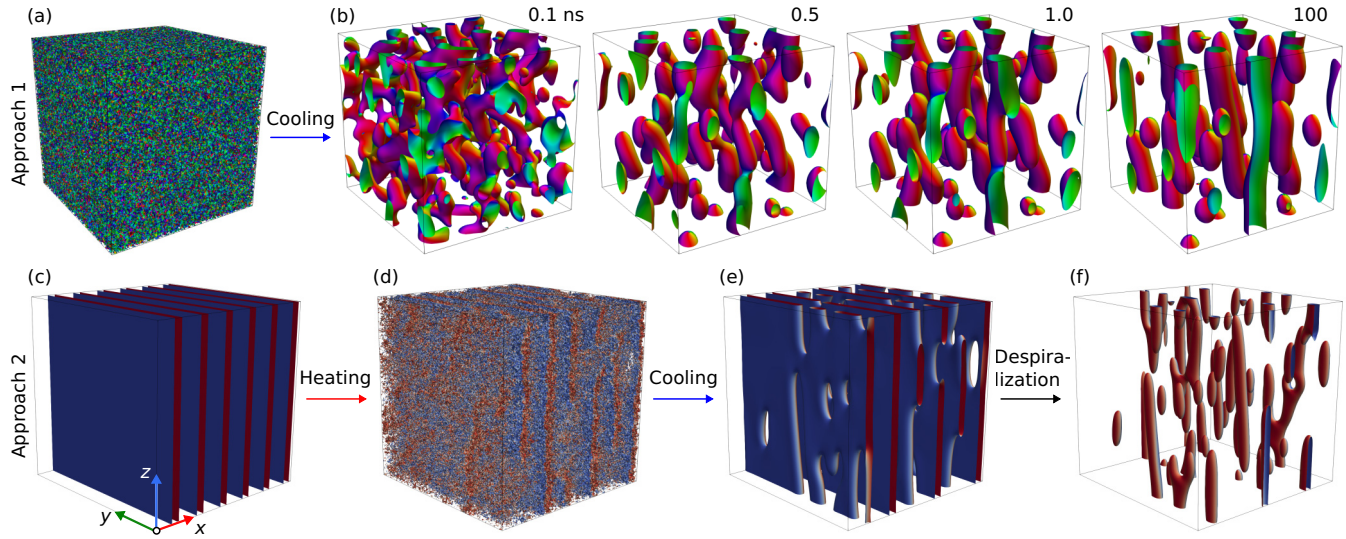

FIG. 2. Magnetic dipole string (DS) nucleation via (a), (b) in-field annealing and (c)–(f) helix breaking. (a) Random spin distribution resembling a paramagnetic state. (b) Sequence of states obtained using LLG simulations at $h = 0.55$ and $u = 0.25$, starting from (a). The simulated box size is $3L_D \times 3L_D \times 3L_D$, discretized into 128^3 cuboids. (c) Helix initial state at $h = 0.57$ and $u = 0.42$. (d) Helix at a temperature of $T \sim 0.9T_C$. (e) State obtained after cooling from (d), showing DSs embedded in the helix. (f) Same as (e) but after the despiralization procedure, which unwinds the helix into a ferromagnetic state. The simulated domain in (c)–(f) is $6L_D \times 6L_D \times 6L_D$, discretized into 256^3 lattice sites. The red-blue color scale in (c)–(f) represents the n_y component of the magnetization. Periodic boundary conditions are applied in all directions.

B. DS stability range

For the study of the stability region of the DS, we constructed a reliable ansatz of its profile that can be used as an initial guess in numerical simulations. Using the parametrization $\mathbf{n} = (\sin\Theta\cos\Phi, \sin\Theta\sin\Phi, \cos\Theta)$, the ansatz for the DS can be written in bispherical coordinates. These coordinates are characterized by two poles at $(0, 0, \pm a/2)$, which coincide with the BP positions:

$$\Theta = \arccos\left[\frac{r^2 - a^2}{\sqrt{(r^2+a^2)^2 - 4a^2z^2}}\right], \quad \Phi = \arctan\frac{y}{x} + \frac{\pi}{2}, \tag{3}$$

where $r = \sqrt{x^2+y^2+z^2}$ denotes the spherical radius and a is the distance between the poles (between the BPs).

Since Eq. (3) gives $\mathbf{n} = (0, 0, 1)$ at $r \to \infty$, it is necessary to rotate both the vector field $\mathbf{n}$ and the spatial coordinates $\mathbf{r}$ to obtain the cone phase vacuum, as described in Ref. [37]. In the case where the DS is embedded in the helix, we place the BPs at $(\pm a/2, 0, 0)$ and apply the spiralization procedure [30], which transforms the FM state into a helix with $\mathbf{q} \parallel \mathbf{e}_x$. For both cases, i.e., DS in the helix and DS in the cone, we provide MUMAX3 scripts in Supplemental Material II, III [27], where the ansatz (3) is implemented.

Starting the energy minimization with the above ansatz, one can obtain a statically stable solution for a DS when B_{ext} and $\mathcal{K}_u$ are in the ranges depicted as semitransparent gray areas in Fig. 1(b). Varying the values of B_{ext} and $\mathcal{K}_u$, we identify the boundaries of the DS stability regions. Note that the DS within the cone and helix phases in Fig. 1(b) represent metastable solutions. This implies that while an isolated DS is a statically stable configuration in these regions, the total energy of the system with a DS is higher than that of the pure cone or helix state. Interestingly, even in the case of the isotropic chiral magnet ($u = 0$), the DS can be stabilized inside the helix phase in a finite range of the applied field, $h \in [0.26, 0.33]$. In this scenario, the DSs are stabilized in a helix, while the ground state of the system is the cone phase. Nevertheless, this indicates that DSs can be experimentally observed even in isotropic chiral magnets, e.g., FeGe [37–40], MnSi [41,42], $Fe_{1-x}Co_xSi$ [43,44], and other B20-type crystals [45]. Experimentally, DSs can be detected using Lorentz transmission electron microscopy (TEM) in plates or films thin enough to be transparent to electrons. For thicker samples and bulk systems, neutron scattering techniques, sensitive to local magnetization inhomogeneities and defects, can provide indirect evidence for the presence of DSs. In both cases, however, the unambiguous identification of the observed magnetic states requires support from micromagnetic simulations.

C. Nucleation of DSs

We consider two approaches to demonstrate the nucleation ability of DSs in the cone and helix phases (Fig. 2). The first approach illustrates DS nucleation via annealing. We begin with a random spin distribution that resembles the paramagnetic phase [Fig. 2(a)]. The system is then cooled using standard Landau-Lifshitz-Gilbert (LLG) simulations, resulting in the configurations shown in Fig. 2(b). This simulation was performed with MUMAX3 [46] using a cubic sample and periodic boundary conditions. After long-term relaxation, the system converges to a mixed state consisting of skyrmion strings and several DSs of different sizes. Similar configurations are consistently observed when the system is cooled

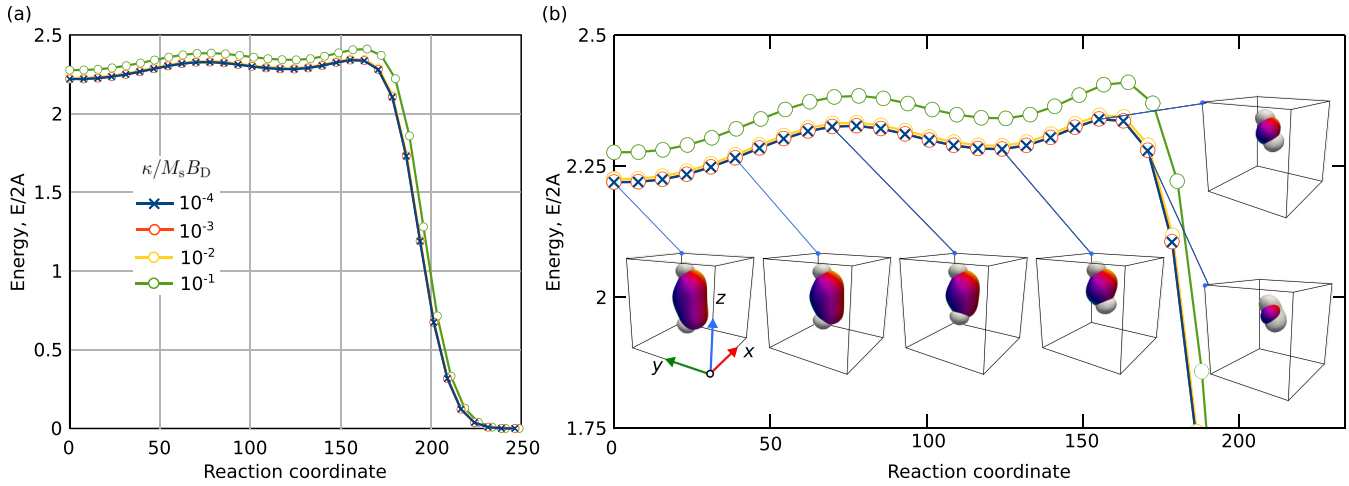

FIG. 3. (a) Minimum energy path (MEP) for dipole string (DS) collapse, shown for different values of the parameter κ in the regularized micromagnetic model. The path connects the stable DS state (leftmost point) to the cone phase state (rightmost point) via the DS's shrinking. (b) Zoomed-in fragment of the MEP from (a), with selected DS configurations visualized at various path images. Isosurfaces correspond to $n_z = 0$, while the white surfaces represent $|\mathbf{n}| = 0.95$. The MEP calculations were performed at $h = 0.55$, $u = 0.25$ in a simulated domain of size $3L_D \times 3L_D \times 3L_D$, discretized with 21 nodes per L_D. The cubic domain in the insets has a side length of $1.5L_D$.

from different initial random states. In these simulations, we frequently observe stable DSs of various lengths corresponding to different equilibrium distances between the BPs. Such behavior of DSs coupled to skyrmion strings has been reported previously [17]. It is important to note that from a topological perspective, all these DSs are identical to the one depicted in Fig. 1(a).

The second approach resembles the method used to nucleate monoaxial skyrmions [47] in experiments [48]. Starting from a helical state [Fig. 2(c)], we perform stochastic LLG simulations using a spin-lattice model and the semi-implicit method [49]. In these simulations, the temperature is set to $T = 1.2J/k_B$, where $J = 2\mathcal{A}$ represents the Heisenberg exchange constant. This temperature is below the Curie temperature of $T_C = 1.345J/k_B$, as estimated in Ref. [17]. After some time, we observed the breaking of several spirals [Fig. 2(d)]. The temperature is then turned off, and the system is gradually cooled. The resulting final state consists of several DSs embedded in the helix [Fig. 2(e)]. To enhance visualization, we applied the despiralization procedure, as described in Ref. [30] [Fig. 2(e)]. Similarly to the first approach, the final state typically comprises skyrmion strings and multiple DSs of varying lengths.

D. Regularized geodesic nudged elastic band method

For the further characterization of DSs, we estimated the energy barriers that protect them from collapse. A representative minimum energy path (MEP), calculated using the geodesic nudged elastic band (GNEB) method [50,51], is shown in Fig. 3. We found that within the standard micromagnetic model where magnetization vectors $\mathbf{n}$ are defined on the $\mathbb{S}^2$-sphere (i.e., ordinary three-dimensional unit vectors), the GNEB method exhibits poor convergence for configurations containing BPs. This issue arises due to the divergence of the effective field in the vicinity of the BP. To address this, we used a regularized micromagnetic model, where the order parameter $\boldsymbol{\nu}$ is defined on the $\mathbb{S}^3$-sphere [52]. The first three components of the four-dimensional vector $\boldsymbol{\nu} = (\nu_1, \nu_2, \nu_3, \nu_4)$ coincide with the magnetization unit vector $\mathbf{n}$, while the fourth component relates to the vector's length:

$$\nu_1 = n_x, \quad \nu_2 = n_y, \quad \nu_3 = n_z, \quad \nu_4^2 = 1 - |\mathbf{n}|^2. \tag{4}$$

In this model, the exchange energy term in Eq. (1) is modified as follows:

$$\mathcal{A} \sum_{i=x,y,z} (\partial_i \mathbf{n})^2 \mapsto \mathcal{A} \sum_{i=x,y,z} (\partial_i \boldsymbol{\nu})^2 + \kappa \nu_4^2, \tag{5}$$

while the DMI and potential energy term remain unchanged. The phenomenological parameter κ in Eq. (5) can be interpreted as a BP localization parameter. In the limit $\kappa \to \infty$ ($\nu_4 \to 0$), the system reduces to the standard micromagnetic model. The regularized model inherently satisfies the condition $|\mathbf{n}| \leqslant 1$, ensuring qualitative consistency with the predictions of the more general quantum-mechanical model [52].

The key aspects of the regularized GNEB method remain identical to those of the standard GNEB method. The entire transition path is discretized into a series of transient states, referred to as images, which interact with each other through forces. The total force acting on each image consists of the effective magnetic field force $\boldsymbol{\beta}_\mathcal{I}$ and the spring force $\boldsymbol{f}_\mathcal{I}$:

$$\boldsymbol{\beta}_\mathcal{I} = -\frac{1}{M_s}\frac{\delta \mathcal{H}}{\delta \boldsymbol{\nu}_\mathcal{I}}, \quad \boldsymbol{f}_\mathcal{I} = k(\rho_{\mathcal{I}+1,\mathcal{I}} - \rho_{\mathcal{I},\mathcal{I}-1})\boldsymbol{\tau}_\mathcal{I}, \tag{6}$$

where $\mathcal{I} \in [1, \mathcal{N}]$ is the image index with $\mathcal{N}$ being the total number of images, k is the spring force constant, ρ is the reaction coordinate (the Euclidian distance between the images), and $\boldsymbol{\tau}_\mathcal{I}$ is the tangent vector. The optimal minimum energy path (MEP) is obtained through iterative minimization of the absolute value of the total force. Details of the RGNEB implementation, including the force minimization algorithm, are provided in the Supplemental Material IV, V [27].

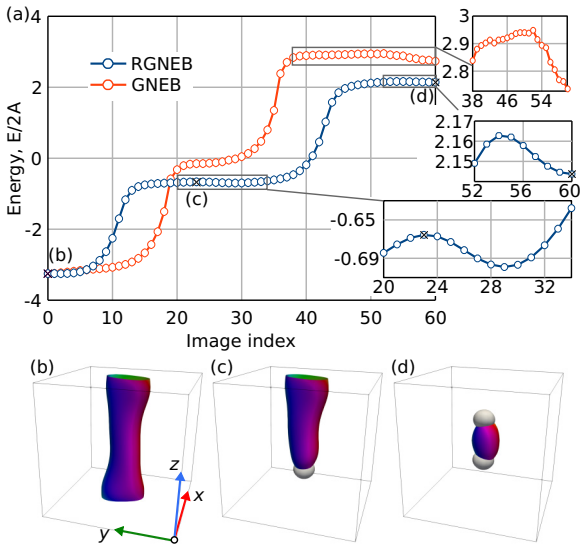

FIG. 4. (a) Minimum energy paths between (b) a skyrmion tube and (d) a dipole string, computed using both the GNEB and RGNEB methods. Calculations were performed on a cubic domain of size $(2.5L_D)^3$, discretized into a mesh of 64^3 cuboids. Periodic boundary conditions were applied in the x and y directions. The external magnetic field was set to $h = 0.65$, and the easy-plane anisotropy parameter to $u = 0.3$. For the RGNEB method, the parameter $\kappa = 10^{-4} M_s B_D$. (b)–(d) Snapshots of the spin texture corresponding to the configurations marked by black crosses on the RGNEB-calculated MEP shown in (a).

Figure 3(a) shows the MEP calculated for four different values of κ. As κ increases and the model approaches the classical micromagnetic model, the energy at each point along the MEP increases while the convergence of the RGNEB method slows down significantly. For $\kappa > 0.1$, achieving reasonable accuracy becomes problematic, as the RGNEB method fails to converge due to the pinning of the BPs in the lattice.

The initial path guess was generated using the ansatz (3), where the distance between the BPs, a, changes linearly along the MEP. For all values of κ, the MEP exhibits two saddle points and one intermediate minimum, corresponding to a more compact but slightly higher-energy DS. A zoomed-in fragment of the MEP is shown in Fig. 3(b), along with system snapshots for selected images where the DS is visualized using two isosurfaces. The color-coded isosurface indicates the shape and size of the DS; the second one highlights the BP positions. The full set of snapshots is available in Supplemental Movie 1 [27].

E. DS nucleation from the skyrmion string

The approach discussed in Sec. III C enables massive nucleation of DSs. To illustrate the possibility of nucleating an individual DS, Fig. 4 shows a MEP between a stable skyrmion and a DS, computed using both the GNEB and RGNEB methods. The existence of such a MEP indicates that, under certain conditions, a transition between these states is feasible, and an individual skyrmion can be converted into a DS. For the GNEB calculations, we used our publicly available extension for MUMAX3 [53]. It is important to note that, in both cases of GNEB and RGNEB, the initial MEP is generated via linear interpolation between the two end states.

At first glance, both methods yield comparable results. However, in addition to differences in the energy barrier heights, the MEP obtained with the RGNEB method reveals an extra intermediate local minimum that is absent in the MEP computed using the standard GNEB method. Furthermore, the motion of BPs under the change in DS size exhibits pinning effects, resulting in abrupt energy variations between adjacent images along the MEP. Although such BP pinning may appear naturally in spin lattice models [57], in the continuum framework, it constitutes an artifact arising from the finite-difference scheme used to approximate derivatives in the micromagnetic Hamiltonian. One may conclude that RGNEB is preferable for studying transitions involving BPs. Supplemental Movies 2 and 3 [27] provide complete sets of spin texture snapshots along the MEPs computed using RGNEB and GNEB, respectively.

Given the finite energy barriers between the skyrmion string and the DS, thermal fluctuations could, in principle, induce such transitions. Similar thermally activated nucleations have been observed for other spin textures [30,54,55]. However, to estimate the temperature range in which such transitions could become experimentally accessible, a more detailed analysis, for example, with transition rate theory [56], is needed.

F. Current-induced motion of DS

The dynamics of DSs can be modeled with the LLG equation:

$$\frac{\partial \mathbf{n}}{\partial t} = -\gamma \mathbf{n} \times \mathbf{B}_{\text{eff}} + \alpha \mathbf{n} \times \frac{\partial \mathbf{n}}{\partial t} + \mathbf{T}, \tag{7}$$

where γ and α are the gyromagnetic ratio and Gilbert damping, respectively. The effective magnetic field is defined as the variational derivative of the Hamiltonian (1), $\mathbf{B}_{\text{eff}} = -(M_s)^{-1}\delta\mathcal{E}/\delta\mathbf{n}$. The torque $\mathbf{T}$ is chosen to model the presence of electric current with density $\mathbf{j}$ via the Zhang-Li mechanism [58]:

$$\mathbf{T} = -\mathbf{n} \times [\mathbf{n} \times (\mathbf{J} \cdot \nabla)\mathbf{n}] - \xi \mathbf{n} \times (\mathbf{J} \cdot \nabla)\mathbf{n}, \tag{8}$$

where ξ is the nonadiabaticity parameter and $\mathbf{J} = \mu_B \mu_0 \boldsymbol{j}/2e\gamma_0 M_s(1+\xi^2)$. By numerically solving Eqs. (7) and (8) in MUMAX3 [46] with a current density $\mathbf{j} = [-15 \times 10^{10} \times f(t), 0, 0]$ A/m^2, we induce the motion of the DS in the xy plane (see Fig. 5). To suppress the excitation of additional modes, we employed a smoothing function, $f(t) \in [0, 1]$, defined as follows [59]:

$$f(t) = 1 - \frac{1 + \exp(-2)}{1 + \exp[2\omega t - 2]}, \quad \omega = 1\,\text{GHz}. \tag{9}$$

To obtain the velocity of a DS, we have first calculated its position $\boldsymbol{r}_c = (r_{x,c}, r_{y,c}, r_{z,c})$, taking into account periodic boundary conditions [60]:

$$r_{i,c} = \frac{L_i}{2\pi} \tan^{-1} \frac{\int \mathcal{N}_{jk} \sin(2\pi r_i/L_i) \mathrm{d}r_i}{\int \mathcal{N}_{jk} \cos(2\pi r_i/L_i) \mathrm{d}r_i} \pm l_i L_i, \tag{10}$$

vskip-3ptwhere the nonrepeating indices $\{i, j, k\} \in \{x, y, z\}$, and $\mathcal{N}_{jk} = \int (1 - n_z) \mathrm{d}r_j \mathrm{d}r_k$. The integers l_i represent the number of times the DS has crossed the domain boundary in

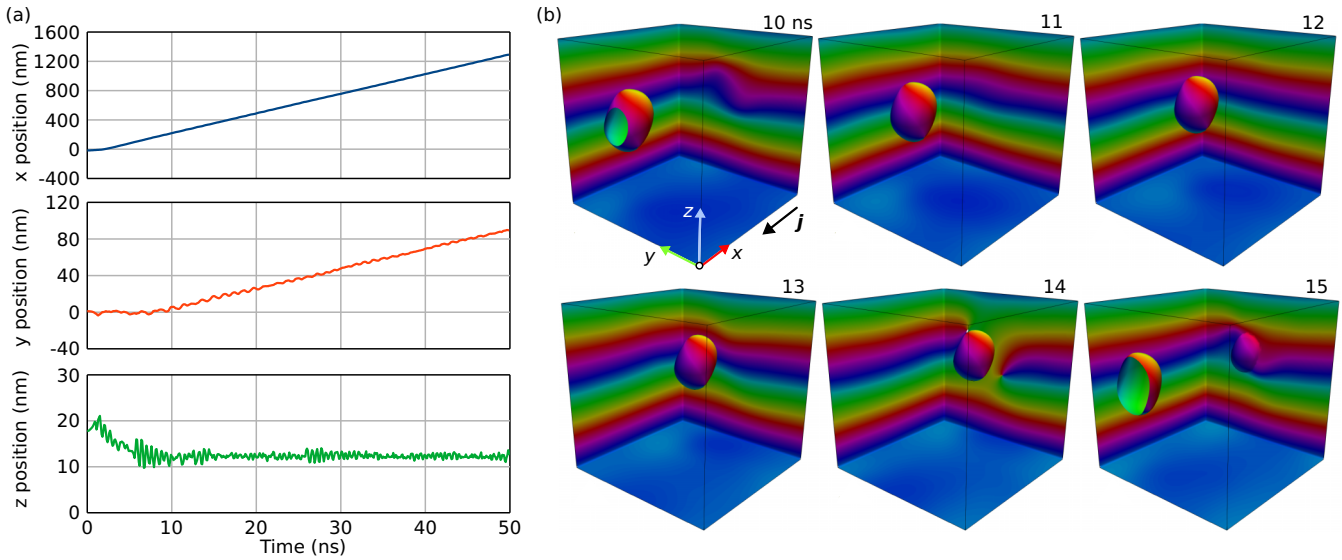

FIG. 5. (a) Temporal evolution of the x, y, and z components of the center of mass of a DS, calculated according to Eq. (10) and based on the numerical solution of the LLG equation [Eqs. (7) and (8)]. (b) Snapshots of the system illustrating the motion of a DS. The stable DS was obtained for the same physical parameters as in Fig. 1(a), and the simulation domain was discretized into 64^3 cuboids.

the x, y, and z directions, respectively. Then, the DS velocity is calculated as the time derivative of its position, $\boldsymbol{v} = \dot{\boldsymbol{r}}_c$. For the chosen current density $\mathbf{j}$, $\alpha = 0.05$, and $\xi = 0.25$, we obtain $\boldsymbol{v} \cong (26.9, 2.16, 0)\,\mathrm{m/s}$.

As we can see from the numerical simulations [Fig. 5(a)], the DS moves with a certain deflection angle $\beta = \arctan(v_y/v_x) > 0$ in the xy plane. This can be easily understood from the fact that the DS represents a fragment of a skyrmion string and is characterized by a nonzero topological charge in some of its z cross sections, which leads to a nonzero skyrmion Hall angle. Snapshots of the system providing a representative picture of the DS motion are given in Fig. 5(b), and the whole dynamics simulation is available in the Supplemental Movie 4 [27].

The DS's translational motion is accompanied by periodic vibrations, which arise from frequent jumps of the BPs between adjacent nodes of the discrete mesh. Similar effects have been previously observed in the current-induced motion of chiral bobbers [61]. These vibrations appear to be a general feature of magnetic textures hosting BPs and become more

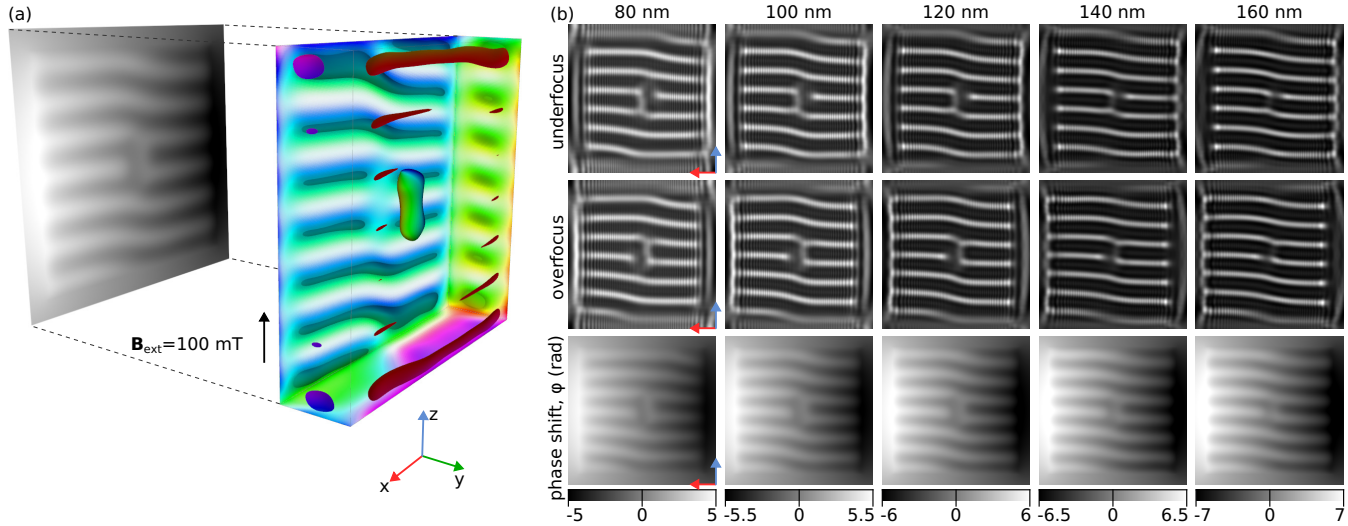

FIG. 6. (a) Schematic illustration of the TEM setup. The electron beam is oriented perpendicular to the FeGe plate, which has dimensions of 500 nm × 500 nm × 120 nm. An external magnetic field is applied along the z axis, in the plane of the plate. The magnetization is shown at the edges of the simulated box and is represented by the isosurface at $m_z = -0.3$. The central dipole string is slightly elongated, with a distance between the Bloch points of $\sim 1.5L_D$. (b) The top two rows display Lorentz TEM images in both overfocus and underfocus conditions (defocus distance: 700 μm) for FeGe plates of varying thickness. The bottom row shows the corresponding electron holography images, which visualize the phase shift of the electron wave. Supplemental Fig. S1 [27] presents similar TEM images for a more compact dipole string with a distance between the Bloch points of $\sim 1L_D$ and stabilized at 150 mT.

pronounced as the mesh density increases. A detailed analysis of the dynamics of solitons hosting BPs lies beyond the scope of this work and will be presented elsewhere [62].

G. Observation of DS in TEM

To demonstrate that DSs can be experimentally detected, we calculated the Lorentz TEM contrast and the electron wave phase shift using a standard method [8]. These calculations were performed using the EXCALIBUR code [63], which enables direct energy minimization and *in situ* computation of Lorentz TEM and phase-shift images. Simulations were carried out for a square-shaped plate with material parameters corresponding to a B20-type FeGe crystal, including the effects of demagnetizing fields. The TEM setup and the simulated domain containing a stable DS are shown in Fig. 6(a), while the resulting Lorentz TEM and electron holography (phase-shift) images are presented in Fig. 6(b).

FeGe possesses negligibly weak magnetocrystalline anisotropy [8]. However, in extended plates, demagnetizing fields effectively induce an easy-plane anisotropy that stabilizes the DS. The DS configuration remains stable under an external magnetic field applied in the sample plane and persists over a wide range of plate thicknesses. For the present geometry, we have estimated the lower stability limit for DS at a plate thickness of approximately L_D, which corresponds to 70 nm in FeGe. For plates equal to or thinner than L_D, DSs become unstable.

We computed Lorentz TEM images in both overfocus and underfocus conditions, as well as phase-shift images, for various plate thicknesses. As these results show, when the thickness increases, detecting DSs may become difficult. However, the characteristic contrast remains clearly visible for plate thicknesses between 80 nm and 160 nm. In addition to TEM, DSs can also be observed using x-ray magnetic microscopy techniques [64].

IV. CONCLUSIONS

In this work, we introduced a model of a bulk chiral magnet where a magnetic dipole string (DS) exists as a truly statically stable soliton. We demonstrated that DSs can be stabilized within the cone or helix phases, or in mixed states coexisting with skyrmion strings. It is shown that uniaxial chiral magnets are promising systems for the experimental observation of DSs when the external magnetic field is applied perpendicular to the hard axis. However, we also show that DSs can be stabilized in isotropic chiral magnets in a certain range of applied magnetic fields. Furthermore, we argue that spontaneous nucleation of DSs can be achieved through controlled annealing of the sample, making this phenomenon experimentally accessible. We demonstrate that DSs can be directly observed in TEM, even in materials lacking easy-plane anisotropy. In particular, we show that DSs can be stabilized in B20-type FeGe due to the effect of shape anisotropy. Moreover, similar to other magnetic solitons, DSs can move under an applied electric current. Finally, we establish that a regularized micromagnetic model provides an adequate framework for describing DSs and can be readily adapted for minimum energy path calculation methods, facilitating further theoretical and computational studies.

ACKNOWLEDGMENTS

The authors acknowledge financial support from the National Research Fund of Luxembourg under Grant No. C22/MS/17415246/DeQuSky and AFR/23/17951349. V.M.K. acknowledges the financial support from the European Unions Horizon 2020 research and innovation programme under the Marie Sklodowska-Curie Grant Agreement No. 101203692 (QUANTHOPF). N.S.K. acknowledges support from the European Research Council under the European Union's Horizon 2020 Research and Innovation Programme (Grant No. 856538—project "3D MAGiC").

DATA AVAILABILITY

The data that support the findings of this article are not publicly available. The data are available from the authors upon reasonable request.

[1] A. N. Bogdanov and D. A. Yablonskii, Thermodynamically stable "vortices" in magnetically ordered crystals. The mixed state of magnets, Sov. Phys. JETP **68**, 101 (1989).

[2] S. Heinze, K. von Bergmann, M. Menzel, J. Brede, A. Kubetzka, R. Wiesendanger, G. Bihlmayer, and S. Blügel, Spontaneous atomic-scale magnetic skyrmion lattice in two dimensions, Nature Phys. **7**, 713 (2011).

[3] L. Powalla, M. T. Birch, K. Litzius, S. Wintz, F. S. Yasin, L. A. Turnbull, F. Schulz, D. A. Mayoh, G. Balakrishnan, M. Weigand, X. Yu, K. Kern, G. Schütz, and M. Burghard, Seeding and Emergence of Composite Skyrmions in a van der Waals Magnet, Adv. Mater. **35**, 2208930 (2023).

[4] M. Hassan, S. Koraltan, A. Ullrich, F. Bruckner, R. O. Serha, K. V. Levchenko, G. Varvaro, N. S. Kiselev, M. Heigl, C. Abert, D. Suess, and M. Albrecht, Dipolar skyrmions and antiskyrmions of arbitrary topological charge at room temperature, Nature Phys. **20**, 615 (2024).

[5] Y. Tokura and N. Kanazawa, Magnetic Skyrmion Materials, Chem. Rev. **121**, 2857 (2021).

[6] K. M. Song, J. S. Jeong, B. Pan *et al.*, Skyrmion-based artificial synapses for neuromorphic computing, Nature Electron. **3**, 148 (2020).

[7] C. Psaroudaki and C. Panagopoulos, Skyrmion qubits: A new class of quantum logic elements based on nanoscale magnetization, Phys. Rev. Lett. **127**, 067201 (2021).

[8] F. Zheng, F. N. Rybakov, N. S. Kiselev, D. Song, A. Kovács, H. Du, S. Blügel, and R. E. Dunin-Borkowski, Magnetic skyrmion braids, Nature Commun. **12**, 5316 (2021).

[9] V. M. Kuchkin and N. S. Kiselev, Homotopy transitions and 3D magnetic solitons, APL Mater. **10**, 071102 (2022).

[10] J. Tang, Y. Wu, W. Wang, L. Kong, B. Lv, W. Wei, J. Zang, M. Tian, and H. Du, Magnetic skyrmion bundles and their current-driven dynamics, Nature Nanotechnol. **16**, 1086 (2021).

[11] F. Zheng, N. S. Kiselev, F. N. Rybakov, L. Yang, W. Shi, S. Blügel, and R. E. Dunin-Borkowski, Hopfion rings in a cubic chiral magnet, Nature (London) **623**, 718 (2023).
[12] E. Feldtkeller, Mikromagnetisch stetige und unstetige Magnetisierungskonfigurationen, Z. Angew. Phys. **19**, 530 (1965).
[13] W. Döring, Point singularities in micromagnetism, J. Appl. Phys. **39**, 1006 (1968).
[14] F. N. Rybakov, A. B. Borisov, S. Blügel, and N. S. Kiselev, New type of stable particlelike states in chiral magnets, Phys. Rev. Lett. **115**, 117201 (2015).
[15] F. Zheng, F. N. Rybakov, A. B. Borisov, D. Song, S. Wang, Zi-An Li, H. Du, N. S. Kiselev, J. Caron, A. Kovács, M. Tian, Y. Zhang, S. Blügel, and R. E. Dunin-Borkowski, Experimental observation of chiral magnetic bobbers in B20-type FeGe, Nature Nanotechnol. **13**, 451 (2018).
[16] M. Redies, F. R. Lux, J.-P. Hanke, P. M. Buhl, G. P. Müller, N. S. Kiselev, S. Blügel, and Y. Mokrousov, Distinct magnetotransport and orbital fingerprints of chiral bobbers, Phys. Rev. B **99**, 140407(R) (2019).
[17] G. P. Müller, F. N. Rybakov, H. Jónsson, S. Blügel, and N. S. Kiselev, Coupled quasimonopoles in chiral magnets, Phys. Rev. B **101**, 184405 (2020).
[18] P. J. Ackerman and I. I. Smalyukh, Diversity of knot solitons in liquid crystals manifested by linking of preimages in torons and hopfions, Phys. Rev. X **7**, 011006 (2017).
[19] M. Grelier, F. Godel, A. Vecchiola, S. Collin, K. Bouzehouane, A. Fert, V. Cros, and N. Reyren, Three-dimensional skyrmionic cocoons in magnetic multilayers, Nature Commun. **13**, 6843 (2022).
[20] G. P. Müller, N. Kiselev, and S. Blügel, Skyrmions and magnetic singularities in confined geometries, lecture MA 54.2 delivered at the DPG Spring Meeting, Dresden, Germany, March 2017.
[21] C. Schütte and A. Rosch, Dynamics and energetics of emergent magnetic monopoles in chiral magnets, Phys. Rev. B **90**, 174432 (2014).
[22] Y. Liu, R. K. Lake, and J. Zang, Binding a hopfion in a chiral magnet nanodisk, Phys. Rev. B **98**, 174437 (2018).
[23] A. S. Savchenko, F. Zheng, N. S. Kiselev, L. Yang, F. N. Rybakov, S. Blügel, and R. E. Dunin-Borkowski, Diversity of states in a chiral magnet nanocylinder, APL Mater. **10**, 061110 (2022).
[24] A. O. Leonov and K. Inoue, Homogeneous and heterogeneous nucleation of skyrmions in thin layers of cubic helimagnets, Phys. Rev. B **98**, 054404 (2018).
[25] A. O. Leonov, Surface anchoring as a control parameter for shaping skyrmion or toron properties in thin layers of chiral nematic liquid crystals and noncentrosymmetric magnets, Phys. Rev. E **104**, 044701 (2021).
[26] M. Azhar, V. P. Kravchuk, and M. Garst, Screw Dislocations in Chiral Magnets, Phys. Rev. Lett. **128**, 157204 (2022).
[27] See Supplemental Material at http://link.aps.org/supplemental/10.1103/PhysRevB.111.174410 for the derivation of the cone-FM transition, MUMAX3 scripts for DS ansatz in cone and helix phases, details of the RGNEB method, and the VPO algorithm.
[28] I. Dzyaloshinsky, A thermodynamic theory of "weak" ferromagnetism of antiferromagnetics, J. Phys. Chem. Solids **4**, 241 (1958).
[29] T. Moriya, Anisotropic superexchange interaction and weak ferromagnetism, Phys. Rev. **120**, 91 (1960).
[30] V. M. Kuchkin, N. S. Kiselev, F. N. Rybakov, I. S. Lobanov, S. Blügel, and V. M. Uzdin, Heliknoton in a film of cubic chiral magnet, Front. Phys. **11**, 1201018 (2023).
[31] E. A. Karhu, U. K. Rößler, A. N. Bogdanov, S. Kahwaji, B. J. Kirby, H. Fritzsche, M. D. Robertson, C. F. Majkrzak, and T. L. Monchesky, Chiral modulations and reorientation effects in MnSi thin films, Phys. Rev. B **85**, 094429 (2012).
[32] R. Voinescu, J.-S. B. Tai, and I. I. Smalyukh, Hopf Solitons in Helical and Conical Backgrounds of Chiral Magnetic Solids, Phys. Rev. Lett. **125**, 057201 (2020).
[33] A. P. Malozemoff and J. C. Slonczewski, *Magnetic Domain Walls in Bubble Materials* (Academic Press, New York, 1979).
[34] N. S. Kiselev, Magnoom software, 2016.
[35] A. S. Savchenko, V. M. Kuchkin, F. N. Rybakov, S. Blügel, and N. S. Kiselev, Chiral standing spin waves in skyrmion lattice, APL Mater. **10**, 071111 (2022).
[36] A. O. Leonov and I. Kézsmárki, Asymmetric isolated skyrmions in polar magnets with easy-plane anisotropy, Phys. Rev. B **96**, 014423 (2017).
[37] H. Du, X. Zhao, F. N. Rybakov, A. B. Borisov, S. Wang, J. Tang, C. Jin, C. Wang, W. Wei, N. S. Kiselev, Y. Zhang, R. Che, S. Blügel, and M. Tian, Interaction of individual skyrmions in a nanostructured cubic chiral magnet, Phys. Rev. Lett. **120**, 197203 (2018).
[38] A. Kovács, J. Caron, A. S. Savchenko, N. S. Kiselev, K. Shibata, Zi-An Li, N. Kanazawa, Y. Tokura, S. Blügel, and R. E. Dunin-Borkowski, Mapping the magnetization fine structure of a lattice of Bloch-type skyrmions in an FeGe thin film, Appl. Phys. Lett. **111**, 192410 (2017).
[39] X. Yu *et al.*, Aggregation and collapse dynamics of skyrmions in a non-equilibrium state, Nature Phys. **14**, 832 (2018).
[40] X. Z. Yu, N. Kanazawa, Y. Onose, K. Kimoto, W. Z. Zhang, S. Ishiwata, Y. Matsui, and Y. Tokura, Near room-temperature formation of a skyrmion crystal in thin-films of the helimagnet FeGe, Nature Mater. **10**, 106 (2011).
[41] S. Mulbauer, B. Binz, F. Jonietz, C. Pfleiderer, A. Rosch, A. Neubauer, R. Georgii, and P. Böni, Skyrmion lattice in a chiral magnet, Science **323**, 915 (2009).
[42] X. Yu, A. Kikkawa, D. Morikawa, K. Shibata, Y. Tokunaga, Y. Taguchi, and Y. Tokura, Variation of skyrmion forms and their stability in MnSi thin plates, Phys. Rev. B **91**, 054411 (2015).
[43] X. Z. Yu, Y. Onose, N. Kanazawa, J. H. Park, J. H. Han, Y. Matsui, N. Nagaosa, and Y. Tokura, Real space observation of a two-dimensional skyrmion crystal, Nature (London) **465**, 901 (2010).
[44] H. S. Park, X. Yu, S. Aizawa, T. Tanigaki, T. Akashi, Y. Takahashi, T. Matsuda, N. Kanazawa, Y. Onose, D. Shindo, A. Tonomura, and Y. Tokura, Observation of the magnetic flux and three-dimensional structure of skyrmion lattices by electron holography, Nature Nanotechnol. **9**, 337 (2014).
[45] N. Kanazawa, S. Seki, and Y. Tokura, Noncentrosymmetric magnets hosting magnetic skyrmions, Adv. Mater. **29**, 1603227 (2017).
[46] A. Vansteenkiste, J. Leliaert, M. Dvornik, M. Helsen, F. Garcia-Sanchez, and B. Van Waeyenberge, The design and verification of MuMax3, AIP Adv. **4**, 107133 (2014).
[47] V. M. Kuchkin and N. S. Kiselev, Skyrmions and antiskyrmions in monoaxial chiral magnets, Phys. Rev. B **108**, 054426 (2023).
[48] L. Li, D. Song, W. Wang, F. Zheng, A. Kovács, M. Tian, R. E.

Dunin-Borkowski, and H. Du, Transformation from magnetic soliton to skyrmion in a monoaxial chiral magnet, Adv. Mater. **35**, 2209798 (2022).

[49] J. H. Mentink, M. V. Tretyakov, A. Fasolino, M. I. Katsnelson, and Th. Rasing, Stable and fast semi-implicit integration of the stochastic LandauLifshitz equation, J. Phys.: Condens. Matter **22**, 176001 (2010).

[50] P. F. Bessarab, V. M. Uzdin, and H. Jónsson, Method for finding mechanism and activation energy of magnetic transitions, applied to skyrmion and antivortex annihilation, Comput. Phys. Commun. **196**, 335 (2015).

[51] P. F. Bessarab, Comment on "Path to collapse for an isolated Néel skyrmion," Phys. Rev. B **95**, 136401 (2017).

[52] V. M. Kuchkin, A. Haller, Š. Liščák, M. P. Adams, V. Rai, E. P. Sinaga, A. Michels, and T. L. Schmidt, Quantum and classical magnetic Bloch points, Phys. Rev. Res. **7**, 013195 (2025).

[53] V. M. Kuchkin, GNEB in MuMax3, https://kuchkin.github.io/gneb.html, 2022.

[54] V. M. Kuchkin, P. F. Bessarab, and N. S. Kiselev, Thermal generation of droplet soliton in chiral magnet, Phys. Rev. B **105**, 184403 (2022).

[55] V. M. Kuchkin, N. S. Kiselev, F. N. Rybakov, and P. F. Bessarab, Tailed skyrmions–An obscure branch of magnetic solitons, Front. Phys. **11**, 1171079 (2023).

[56] P. F. Bessarab, G. P. Müller, I. S. Lobanov, F. N. Rybakov, N. S. Kiselev, H. Jónsson, V. M. Uzdin, S. Blügel, L. Bergqvist, and A. Delin, Lifetime of racetrack skyrmions, Sci. Rep. **8**, 3433 (2018).

[57] S. K. Kim and O. Tchernyshyov, Pinning of a Bloch point by an atomic lattice, Phys. Rev. B **88**, 174402 (2013).

[58] S. Zhang and Z. Li, Roles of nonequilibrium conduction electrons on the magnetization dynamics of ferromagnets, Phys. Rev. Lett. **93**, 127204 (2004).

[59] V. M. Kuchkin, B. Barton-Singer, P. F. Bessarab, and N. S. Kiselev, Symmetry-governed dynamics of magnetic skyrmions under field pulses, Commun. Phys. **8**, 26 (2025).

[60] V. M. Kuchkin, K. Chichay, B. Barton-Singer, F. N. Rybakov, S. Blügel, B. J. Schroers, and N. S. Kiselev, Geometry and symmetry in skyrmion dynamics, Phys. Rev. B **104**, 165116 (2021).

[61] Z. Gong, J. Tang, S. S. Pershoguba, Z. Xie, R. Sun, Y. Li, X. Yang, J. Liu, W. Zhang, X. Zhang, W. He, H. Du, J. Zang, and Z.-H. Cheng, Current-induced dynamics and tunable spectra of a magnetic chiral bobber, Phys. Rev. B **104**, L100412 (2021).

[62] V. M. Kuchkin, A. Haller, Š. Liščák, A. Michels, T. L. Schmidt, and N. S. Kiselev (unpublished).

[63] F. N. Rybakov and E. Babaev, Excalibur software, http://quantumandclassical.com/excalibur/.

[64] C. Donnelly, M. Guizar-Sicairos, V. Scagnoli, S. Gliga, M. Holler, J. Raabe, and L. J. Heyderman, Three-dimensional magnetization structures revealed with X-ray vector nanotomography, Nature (London) **547**, 328 (2017).

Supplemental Material for "Stability and Nucleation of Dipole Strings in Uniaxial Chiral Magnets"

Vladyslav M. Kuchkin,[1,*] Nikolai S. Kiselev,[2] Andreas Haller,[1]
Štefan Liščák,[1] Andreas Michels,[1] and Thomas L. Schmidt[1]

[1] *Department of Physics and Materials Science, University of Luxembourg, L-1511 Luxembourg, Luxembourg*
[2] *Peter Grünberg Institute, Forschungszentrum Jülich and JARA, 52425 Jülich, Germany*

I. CONE-FM TRANSITION

By performing the nondimensionalization in Hamiltonian (1) as described in the main text, one can obtain the functional in the following form:

$$\frac{\mathcal{E}(\mathbf{n})}{2\mathcal{A}} = \int \left[\frac{(\nabla \mathbf{n})^2}{2} + 2\pi \mathbf{n} \cdot \nabla \times \mathbf{n} + 4\pi^2 \left(u n_x^2 - h n_z \right) \right] \mathrm{d}V. \tag{1}$$

To satisfy the constraint $|\mathbf{n}| = 1$, we can employ parametrization with the spherical angles (Θ, Φ) as $\mathbf{n} = (\sin\Theta\cos\Phi, \sin\Theta\sin\Phi, \cos\Theta)$. In the case of the cone, the angles depend only on the z coordinate. The Euler-Lagrange (EL) equations followed from $\delta\mathcal{E} = 0$ have the form:

$$\begin{cases} \left(\frac{1}{2}\left(\Phi'\right)^2 - 2\pi\Phi' - 4\pi^2 u \cos^2\Phi \right) \sin 2\Theta - \Theta'' + 4\pi^2 h \sin\Theta = 0, \\ \left(4\pi^2 u \sin 2\Phi - \Phi'' \right) \sin^2\Theta - \Theta' \left(\Phi' - 2\pi\right) \sin 2\Theta = 0. \end{cases} \tag{2}$$

For $u = 0, h \in [0,1]$, the analytic solution for the cone phase writes as $\mathbf{n}_\mathrm{c} = (\sin\Theta_\mathrm{c}\cos(2\pi z + \phi_0), \sin\Theta_\mathrm{c}\sin(2\pi z + \phi_0), \cos\Theta_\mathrm{c})$, where $\cos\Theta_\mathrm{c} = h$ and ϕ_0 may take arbitrary value. At $u > 0$, the analytic solution of (2) corresponding to the cone phase is not known and can be found only numerically. However, the critical magnetic field corresponding to the transition to the FM state can be found analytically. To obtain this solution, we parametrize magnetization with stereographic projections, (γ_1, γ_2), as:

$$\mathbf{n} = \left(\frac{2\gamma_1}{1+\gamma_1^2+\gamma_2^2}, \frac{2\gamma_2}{1+\gamma_1^2+\gamma_2^2}, \frac{1-\gamma_1^2-\gamma_2^2}{1+\gamma_1^2+\gamma_2^2} \right). \tag{3}$$

In these projections, the solution for the cone phase at $u = 0$ can be written as:

$$\gamma_1 + i\gamma_2 = e^{i(2\pi z + \phi_0)} \tan\frac{\Theta_\mathrm{c}}{2}. \tag{4}$$

From this, we can deduce, at the transition to the FM state, $h = h^\mathrm{cr}$, one has $\Theta_\mathrm{c} \to 0$, or equivalently, $\gamma_1 \to 0$ and $\gamma_2 \to 0$. Plugging (3) into (1), we derive the EL equations for (γ_1, γ_2) and linearize them at $\gamma_1 \ll 1$ and $\gamma_2 \ll 1$:

$$\begin{aligned} &4\pi^2 \left(h^\mathrm{cr} - 2u\right)\gamma_1 - 4\pi\gamma_2' - \gamma_1'' = 0, \\ &4\pi^2 h^\mathrm{cr}\gamma_2 + 4\pi\gamma_1' - \gamma_2'' = 0, \end{aligned} \tag{5}$$

which is equivalent to a single higher-order linear equation:

$$\gamma_1^{(4)} + 8\pi^2 \left[2 - h^\mathrm{cr} + u\right]\gamma_1'' + 16\pi^4 h^\mathrm{cr}\left(h^\mathrm{cr} - 2u\right)\gamma_1 = 0. \tag{6}$$

Characteristic polynomial for (6):

$$\lambda^4 + 8\pi^2 \left[2 - h^\mathrm{cr} + u\right]\lambda^2 + 16\pi^4 h^\mathrm{cr}\left(h^\mathrm{cr} - 2u\right) = 0, \tag{7}$$

has four solutions:

$$\lambda = \pm 2\pi \sqrt{h^\mathrm{cr} - 2 - u \pm \sqrt{\left(2+u\right)^2 - 4h^\mathrm{cr}}}, \tag{8}$$

where signs $\pm$ in front of both square roots have to be treated separately. The instability criterion for the cone phase is obtained by setting the expression under the inner square root to zero and reads:

$$h^\mathrm{cr} = \left(1 - \frac{u}{2}\right)^2, \; u \in [0,2]. \tag{9}$$

The latter equation means one can find a stable cone phase for all $u \in [0,2]$ and $0 \leq h < h^\mathrm{cr}$.

II. MUMAX3 SCRIPT FOR DS ANSATZ IN CONE PHASE

```
OutputFormat = OVF2_BINARY
/************* Material constants (FeGe) ************************/
Ms := 384e3; Msat = Ms  // saturation magnetization [A/m]
LD := 70.0e-9           // spiral period             [nm]
A := 4.0e-12            // exchange stifness         [J/m]
DMI := 4.0*pi*A/LD      // DMI                       [J/m^2]
Aex = A
Dbulk = DMI
BD := DMI * DMI / (2 * A * Ms)
/******* Easy-plane anisotropy and External magnetic field *****/
anisU = vector (1 , 0 , 0)
Ku1 = -0.25 * 2 * DMI * DMI / (4 * A )
B := 0.55 * BD
B_ext = vector(0, 0, B)
// Ku1 and B_ext correspond to equilibrium spiral period:
// L = 1.016232685 * LD;
/********** Sets GridSize, CellSize and PBC ******************/
n := 128;
SetGridSize(n, n, n);
L := 3.0 * 1.016232685 * LD;
d := L/n;
SetCellSize(d, d, d);
EnableDemag = false
SetPBC(1, 1, 1)
openbc = false
// /*************** Initial state ***************************/
// Globule ansatz in bispherical coordinates
aBP := 0.3; //distance between Bloch points
Th  := 0.8;  //cone phase angle
for ix:=0; ix<n; ix++{
    for iy:=0; iy<n; iy++{
        for iz:=0; iz<n; iz++{
            rx := -1.5 + 3.0*ix/n + 1e-6 //to exclude division by 0
            ry := -1.5 + 3.0*iy/n + 1e-6 //to exclude division by 0
            rz := -1.5 + 3.0*iz/n + 1e-6 //to exclude division by 0
            r := sqrt(rx*rx+ry*ry+rz*rz);
            f := atan2(ry,rx)
            Q := sqrt((r*r+aBP*aBP)*(r*r+aBP*aBP) - 4.0*rz*rz*aBP*aBP);
            theta := acos((r*r-aBP*aBP)/Q);
            phi   := f + 0.5*pi - 2.0*pi*rz;
            mx := sin(theta)*cos(phi)*cos(Th) - cos(theta)*sin(Th);
            mz := cos(theta)*cos(Th) + sin(theta)*cos(phi)*sin(Th);
            my := sin(theta)*sin(phi);
            m1 := mx*cos(2.0*pi*rz) - my*sin(2.0*pi*rz);
            m2 := my*cos(2.0*pi*rz) + mx*sin(2.0*pi*rz);
            m3 := mz;
            mnew:=vector(m1, m2, m3);
            m.SetCell(ix, iy, iz, mnew);
        }
    }
}
/*************** Running minimization ***********************/
save(m)
relax()
minimize()
save(m)
```

III. MUMAX3 SCRIPT FOR DS ANSATZ IN HELICOIDAL PHASE

```
OutputFormat = OVF2_BINARY
/************ Material constants (FeGe) ************************/
Ms := 384e3; Msat = Ms  // saturation magnetization [A/m]
LD := 70.0e-9           // spiral period             [nm]
A := 4.0e-12            // exchange stiffness        [J/m]
DMI := 4.0*pi*A/LD      // DMI                       [J/m^2]
Aex = A
Dbulk = DMI
BD := DMI * DMI / (2 * A * Ms)
/******* Easy-plane anisotropy and External magnetic field *****/
anisU = vector (1 , 0 , 0)
Ku1 = -0.42 * 2 * DMI * DMI / (4 * A )
B := 0.57 * BD
B_ext = vector(0, 0, B)
// Ku1 and B_ext correspond to equilibrium spiral period:
// L = 1.371152 * LD;
/********** Sets GridSize, CellSize and PBC ******************/
n := 128;
SetGridSize(n, n, n);
L := 3.0 * 1.371152 * LD;
d := L/n;
SetCellSize(d, d, d);
EnableDemag = false
SetPBC(1, 1, 1)
openbc = false
// /*************** Initial state ***************************/
// Globule ansatz in bispherical coordinates
aBP := 0.4; //distance between Bloch points
for ix:=0; ix<n; ix++{
    for iy:=0; iy<n; iy++{
        for iz:=0; iz<n; iz++{
            rx := -1.5 + 3.0*ix/n + 1e-6 //to exclude division by 0
            ry := -1.5 + 3.0*iy/n + 1e-6 //to exclude division by 0
            rz := -1.5 + 3.0*iz/n + 1e-6 //to exclude division by 0
            r := sqrt(rx*rx+ry*ry+rz*rz);
            f := -atan2(ry,rz)
            Q := sqrt((r*r+aBP*aBP)*(r*r+aBP*aBP) - 4.0*rx*rx*aBP*aBP);
            theta := acos((r*r-aBP*aBP)/Q);
            phi   := f + 0.5*pi;
            mx := sin(theta)*cos(phi);
            my := sin(theta)*sin(phi);
            mz := cos(theta);
            m1 := mx
            m2 := -my*cos(2*pi*rx)+mz*sin(2*pi*rx)
            m3 := -mz*cos(2*pi*rx)-my*sin(2*pi*rx)
            mnew:=vector(m1, m2, m3);
            m.SetCell(ix, iy, iz, mnew);
        }
    }
}
/*************** Running minimization ***********************/
save(m)
relax()
minimize()
save(m)
```

IV. DETAILS OF THE REGULARIZED GNEB METHOD

Let us denote the set of images (transient states) along the path as $\mathcal{M} = \{\mathcal{M}_\mathcal{I}, \mathcal{I} \in [1, \mathcal{N}]\}$, where $\mathcal{M}_\mathcal{I} = \{\boldsymbol{\nu}_{i,\mathcal{I}} \,|\, i \in [1, N]\}$ represents the $\mathcal{I}$-th of $\mathcal{N}$ images. Each image contains N four-dimensional vectors $\boldsymbol{\nu}$, which define the state. We define the distance between two images, $\mathcal{I}$ and $\mathcal{J}$, as the Euclidean distance:

$$\rho_{\mathcal{I},\mathcal{J}} = \sqrt{\sum_{i=1}^{N}\sum_{j=1}^{4}\left(\nu_{\mathcal{I},i,j} - \nu_{\mathcal{J},i,j}\right)^2}. \tag{10}$$

In practice, we need to know the distance ρ between neighboring images only, *i.e.*, $\mathcal{J} = \mathcal{I} - 1$ or $\mathcal{J} = \mathcal{I} + 1$. All intermediate images, $1 < \mathcal{I} < \mathcal{N}$, are *movable* and must be optimized using the algorithm described below. Meanwhile, the first $\mathcal{I} = 1$ and last $\mathcal{I} = \mathcal{N}$ images are stationary states corresponding to the local minima of the Hamiltonian. For further convenience, we define the following projection operator:

$$\mathcal{P}(\mathbf{a}, \mathbf{b}) = \mathbf{b} - (\mathbf{a} \cdot \mathbf{b})\mathbf{a}, \tag{11}$$

which subtracts from a vector $\mathbf{b}$ its projection onto a vector $\mathbf{a}$.

Each image (state) $\mathcal{I}$ is characterized by the energy, $e_\mathcal{I}$, that for the regularized micromagnetic Hamiltonian is calculated using Eqs. (1) and (5) in the main text. After calculating the energies, one can determine the *tangent* vectors:

$$\mathbf{T}^*_{\mathcal{I},i} = \begin{cases} \boldsymbol{\nu}_{\mathcal{I}+1,i} - \boldsymbol{\nu}_{\mathcal{I},i},\ e_{\mathcal{I}-1} < e_\mathcal{I} < e_{\mathcal{I}+1}, \\ \boldsymbol{\nu}_{\mathcal{I},i} - \boldsymbol{\nu}_{\mathcal{I}-1,i},\ e_{\mathcal{I}-1} > e_\mathcal{I} > e_{\mathcal{I}+1}, \\ \boldsymbol{\nu}_{\mathcal{I}+1,i} - \boldsymbol{\nu}_{\mathcal{I},i} + c(\boldsymbol{\nu}_{\mathcal{I},i} - \boldsymbol{\nu}_{\mathcal{I}-1,i}),\ e_{\mathcal{I}+1} > e_{\mathcal{I}-1}, \\ c(\boldsymbol{\nu}_{\mathcal{I}+1,i} - \boldsymbol{\nu}_{\mathcal{I},i}) + \boldsymbol{\nu}_{\mathcal{I},i} - \boldsymbol{\nu}_{\mathcal{I}-1,i},\ e_{\mathcal{I}+1} < e_{\mathcal{I}-1}, \end{cases} \qquad c = \frac{\min\left(|e_{\mathcal{I}+1} - e_\mathcal{I}|, |e_{\mathcal{I}-1} - e_\mathcal{I}|\right)}{\max\left(|e_{\mathcal{I}+1} - e_\mathcal{I}|, |e_{\mathcal{I}-1} - e_\mathcal{I}|\right)}, \tag{12}$$

which must then be projected and normalized:

$$\mathbf{T}_{\mathcal{I},i} = \mathcal{P}\left(\boldsymbol{\nu}_{\mathcal{I},i}, \mathbf{T}^*_{\mathcal{I},i}\right), \quad \boldsymbol{\tau}_{\mathcal{I},i} = \mathbf{T}_{\mathcal{I},i} \Big/ \sqrt{\sum_{i=1}^{N}\left(\mathbf{T}_{\mathcal{I},i}\right)^2}. \tag{13}$$

The spring force, which ensures the equidistant distribution of images along the path, is given by:

$$\boldsymbol{f}_{\mathcal{I},i} = k(\rho_{\mathcal{I}+1,\mathcal{I}} - \rho_{\mathcal{I},\mathcal{I}-1})\ \boldsymbol{\tau}_{\mathcal{I},i}, \tag{14}$$

where k is the spring stiffness constant. The total force acting on the image $\mathcal{I}$ also includes components arising from the Hamiltonian, which have to be projected out into the tangent vectors:

$$\boldsymbol{g}_{\mathcal{I},i} = \mathcal{P}\left(\boldsymbol{\tau}_{\mathcal{I},i}, \boldsymbol{\beta}_{\mathcal{I},i}\right), \tag{15}$$

where $\boldsymbol{\beta}_{\mathcal{I},i} = -\dfrac{1}{M_\mathrm{s}}\dfrac{\delta\mathcal{H}}{\delta\boldsymbol{\nu}_{\mathcal{I},i}}$ is the effective field vector. Thus, the total force in the RGNEB method is written as

$$\mathcal{F}_{\mathcal{I},i} = \mathcal{P}\left(\boldsymbol{\nu}_{\mathcal{I},i}, \boldsymbol{f}_{\mathcal{I},i} + \boldsymbol{g}_{\mathcal{I},i}\right). \tag{16}$$

In the case of endpoints ($\mathcal{I} = 1$ and $\mathcal{I} = \mathcal{N}$), the force (16) includes the effective field only:

$$\mathcal{F}_{\mathcal{I},i} = \mathcal{P}\left(\boldsymbol{\nu}_{\mathcal{I},i}, \boldsymbol{\beta}_{\mathcal{I},i}\right). \tag{17}$$

In both formulas, Eqs. (16), (17), the additional projection is used due to the convenience, as at the equilibrium points one has $\boldsymbol{\nu}_{\mathcal{I},i} \parallel \boldsymbol{\beta}_{\mathcal{I},i}$ or equivalently a zero force, $|\mathcal{F}_{\mathcal{I},i}| = 0$.

The primary goal of the RGNEB is to minimize all forces, achieved using the algorithm and convergence criteria described in the next section.

V. VELOCITY PROJECTION OPTIMIZATION

Denoting the set of all forces $\mathcal{F} = \{\mathcal{F}_\mathcal{I}, \mathcal{I} \in [1, \mathcal{N}]\}$ where $\mathcal{F}_\mathcal{I} = \{\mathcal{F}_{i,\mathcal{I}}, i \in [1, N]\}$, the velocity projection optimization (VPO) represents the descent method, $\mathcal{M} \mapsto \mathcal{M} + \omega\mathcal{F}$, with an adaptive change of the weight parameter, ω. The

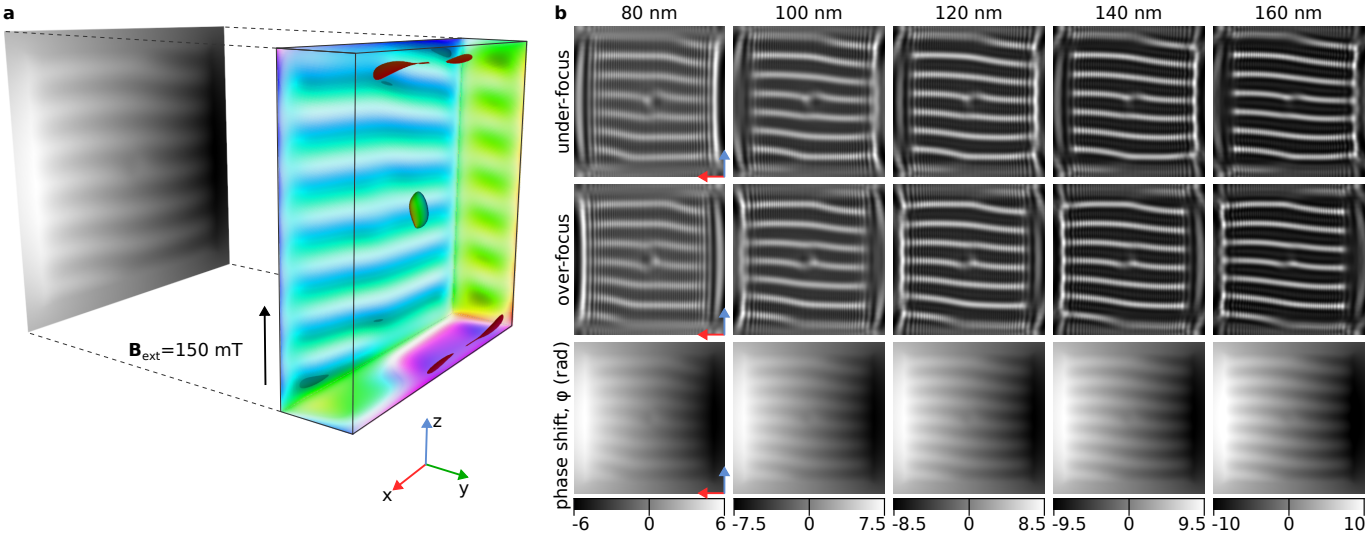

FIG. 1. (a) The same as Fig. 5 in the main text but for dipole string at external field of 150 mT. The exception is the thinnest plate of 80 nm, where the dipole string collapses at 150 mT. In this case, the Lorentz TEM images and phase shift images were calculated at 140 mT.

convergence criterion for the method is defined simply as:

$$|\mathcal{F}| = \frac{1}{N(\mathcal{N}-2)}\sqrt{\sum_{\mathcal{I}=2}^{\mathcal{N}-1}\sum_{i=1}^{N}\left(\mathcal{F}_{\mathcal{I},i}\right)^2} < \epsilon, \tag{18}$$

meaning that the average force is less than a given small ϵ. The VPO algorithm is given as follows:

```
INPUT:  magnetization array M0;  tolerance tol; step dt; mass m;
        maximal number of steps MaxIter;

OUTPUT: magnetization array M1;

Step 1: Set velocity array to zero: V=0
Step 2: for i = 1,2,...,MaxIter do Step 3.
Step 3: Calculate forces, F, according  to Eq.(22) and Set ff = Dot(F,F)
        IF sqrt(ff)/size(M0) < tol
            OUTPUT M0 and STOP
        ELSE do Steps 4-8
Step 4: Set vf = Dot(V+F*dt/2m,F)
        IF vf <= 0
            Set V = 0
        ELSE
            Set V = F*vf/ff
Step 5: Obtain the descent direction: D = V + F*dt/2m
Step 6: Perform the descent step:  M1 = M0 + dt*D
Step 7: Set velocity projected on M1:  V = D*Dot(M0,M1)-M0*Dot(M1,D)
Step 8: Set magnetization: M0 = M1 and  do Step 3
Step 9: PRINT(ERROR: The maximal number of iterations was exceeded!)
        OUTPUT M0
Step 10:STOP.
```

In the above listing, we optimize the movable images only because the endpoint images are the local minimum states or have to be separately optimized according to any available minimization procedure. To minimize the endpoints with the VPO method in parallel to the RGNEB calculations, one has to account for possible different values for the weight parameter ω for both subroutines.